Journal of ELECTRONIC MATERIALS, Vol. 47, No. 2, 2018
https://doi.org/10.1007/s11664-017-5978-7

TOPICAL COLLECTION: 59TH ELECTRONIC MATERIALS CONFERENCE 2017

Free-Standing β-Ga_2O_3 Thin Diaphragms

XU-QIAN ZHENG,[1] JAESUNG LEE,[1] SUBRINA RAFIQUE,[1] LU HAN,[1] CHRISTIAN A. ZORMAN,[1] HONGPING ZHAO,[1] and PHILIP X.-L. FENG[1,2]

1.—Department of Electrical Engineering and Computer Science, Case School of Engineering, Case Western Reserve University, 10900 Euclid Avenue, Cleveland, OH 44106, USA. 2.—e-mail: philip.feng@case.edu

Free-standing, very thin, single-crystal β-gallium oxide (β-Ga_2O_3) diaphragms have been constructed and their dynamical mechanical properties characterized by noncontact, noninvasive optical measurements harnessing the multimode nanomechanical resonances of these suspended nanostructures. We synthesized single-crystal β-Ga_2O_3 using low-pressure chemical vapor deposition (LPCVD) on a 3C-SiC epilayer grown on Si substrate at temperature of 950°C for 1.5 h. The synthesized single-crystal nanoflakes had widths of $\sim$ 2 μm to 30 μm and thicknesses of $\sim$ 20 nm to 140 nm, from which we fabricated free-standing circular drumhead β-Ga_2O_3 diaphragms with thicknesses of $\sim$ 23 nm to 73 nm and diameters of $\sim$ 3.2 μm and $\sim$ 5.2 μm using a dry stamp-transfer technique. Based on measurements of multiple flexural-mode mechanical resonances using ultrasensitive laser interferometric detection and performing thermal annealing at 250°C for 1.5 h, we quantified the effects of annealing and adsorption of atmospheric gas molecules on the resonant characteristics of the diaphragms. Furthermore, we studied the effects of structural nonidealities on these free-standing β-Ga_2O_3 nanoscale diaphragms. We present extensive characterization of the mechanical and optical properties of free-standing β-Ga_2O_3 diaphragms, paving the way for realization of resonant transducers using such nanomechanical structures for use in applications including gas sensing and ultraviolet radiation detection.

Key words: β-Gallium oxide (β-Ga_2O_3), suspended nanostructure, nanomechanics, resonance, nanoelectromechanical systems (NEMS), thermal annealing

INTRODUCTION

Wide-bandgap (WBG) semiconductors, such as silicon carbide (SiC) and gallium nitride (GaN), are widely considered to be increasingly important candidates with great promise for use in development of semiconductor power electronics with better miniaturization and scaling perspectives, as well as devices and integrated systems for applications at high temperature and in other harsh environments. Such expectations are derived largely from their WBG nature and the superior electrical properties they offer over those provided by conventional silicon (Si) devices.[1] In addition to such outstanding electrical properties, WBG semiconductors also offer advantages for enabling functional components in micro/nanoelectromechanical systems (MEMS/NEMS), including higher Young's modulus for higher frequencies, novel and engineerable electromechanical and optomechanical coupling effects, a wide range of insulating, semiconducting, and conducting characteristics based on doping, etc.[2] β-Ga_2O_3, which possesses an ultrawide bandgap (UWBG), has recently drawn increasing attention as a material for use in future generations of power electronics,[3–5] ultraviolet optoelectronics, and other

(Received August 8, 2017; accepted November 19, 2017; published online December 28, 2017)

applications beyond the capabilities of conventional WBG materials (such as SiC and GaN).[6,7] Thanks to its UWBG ($E_g \approx 4.5$ eV to 4.9 eV),[8,9] power devices made of β-Ga_2O_3 may exhibit breakdown voltages even higher than those of devices based on mainstream WBG 4H-SiC and GaN materials.[10–14] In addition to its electrical properties, β-Ga_2O_3 possesses excellent mechanical properties (with Young's modulus $E_{Y,\beta\text{-}Ga2O3}$ of 232 GPa),[15,16] and outstanding chemical and thermal stability (with melting point of 1820°C).[17] β-Ga_2O_3 also offers reversible response to oxidation and reduction gases,[18] enabling gas sensing applications. Furthermore, bulk,[19–22] thin-film,[23,24] and nanostructure[25–28] β-Ga_2O_3 synthesis methods are readily available for construction of β-Ga_2O_3 micro- and nanomechanical devices. These properties provide intriguing new opportunities to enable next-generation MEMS and NEMS devices using β-Ga_2O_3 crystal, being suitable for operation in harsh and extreme environments. Exploration of the mechanical properties of β-Ga_2O_3 and development of β-Ga_2O_3 mechanical devices are also essential to supplement the rapidly burgeoning field of β-Ga_2O_3 electronics, toward future integration of critical mechanical functions into electronics. To date, the majority of such effort has focused on studying growth, electrical characterization, and prototyping electronic devices, whereas the mechanical properties of β-Ga_2O_3, especially in micro/nanoscale platforms, remain to be studied.

We describe herein realization of free-standing, very thin, single-crystal β-Ga_2O_3 diaphragms, and characterization of the mechanical properties of β-Ga_2O_3 through noncontact, noninvasive optical measurements, by harnessing the ultrasensitive readout of the multiple flexural-mode nanomechanical resonances of these suspended β-Ga_2O_3 nanostructures. We synthesized β-Ga_2O_3 single-crystal nanoflakes using a low-pressure chemical vapor deposition (LPCVD) method on a 3C-SiC epilayer on Si substrate. Using a dry transfer technique, we then constructed free-standing β-Ga_2O_3 nanodiaphragms with thicknesses from $\sim$ 23 nm to 73 nm and diameters of $\sim$ 3.2 μm and $\sim$ 5.2 μm. After device fabrication, we used scanning electron microscopy (SEM) and atomic force microscopy (AFM) to observe the geometry and morphology of the fabricated diaphragms, and Raman spectroscopy to confirm the crystal quality of the β-Ga_2O_3 nanoflakes. Employing an ultrasensitive laser interferometry system, we measured the flexural-mode nanomechanical resonances to investigate the mechanical properties of such structures. From the undriven thermomechanical noise spectra of the diaphragms, we detected multimode resonances up to the sixth mode. In addition, we measured resonance frequency and quality (Q) factor changes after thermal annealing to observe gas adsorption effects on the β-Ga_2O_3 nanodiaphragms. We further investigated the impact of subtle structural defects upon the resonance characteristics of the diaphragms.

EXPERIMENTAL PROCEDURES

β-Ga_2O_3 Nanoflake Synthesis

Construction of the suspended β-Ga_2O_3 nanodiaphragms started with synthesis of low-dimensional β-Ga_2O_3 nanoflakes using an LPCVD method. The nanoflakes were synthesized on a 3C-SiC epilayer on Si substrate in a conventional tube furnace with programmable gas flow rate and temperature controllers. Over a 1.5-h period at growth temperature of 950°C, using high-purity Ga pellets (Alfa Aesar, 99.99999%) as source material and O_2 as gaseous precursor, formation of β-Ga_2O_3 proceeded stepwise from β-Ga_2O_3 nanoclusters to β-Ga_2O_3 nanorods then nanoflakes, without use of any foreign catalyst.[29] The as-grown nanoflakes had widths of $\sim$ 2 μm to 30 μm and thicknesses of $\sim$ 20 nm to 140 nm. This method represents a new means to achieve very thin β-Ga_2O_3 flakes with smoother edges, as compared with mechanically exfoliated flakes.[5,30–32]

Suspended β-Ga_2O_3 Nanodiaphragm Fabrication

To fabricate suspended β-Ga_2O_3 nanodiaphragm structures, we used a dry transfer method to relocate the synthesized nanoflakes to predefined circular microtrenches. Large arrays of microtrenches were lithographically defined and fabricated on a 290-nm SiO_2-on-Si substrate before transfer. The SiO_2 layer was patterned with circular microtrenches using photolithography, then etched by reactive-ion etching (RIE). The depth of the resulting SiO_2 microtrenches is 290 nm in this work, and the nominal values for the microtrench diameters in the design are 3 μm and 5 μm (corresponding to actual diameters of $\sim$ 3.2 μm and $\sim$ 5.2 μm measured after fabrication).

Using the synthesized β-Ga_2O_3 nanoflakes, we fabricated suspended β-Ga_2O_3 nanostructures by employing an all-dry transfer technique (Fig. 1). With the assistance of thermal release tape, we picked up the β-Ga_2O_3 nanoflakes from the as-grown samples and thermally released the flakes onto the prefabricated substrate with predefined circular microtrenches. Using this method, we fabricated β-Ga_2O_3 circular drumhead resonators with diameters of $\sim$ 3.2 μm and $\sim$ 5.2 μm (Fig. 2, showing 5 out of 10 devices demonstrated in this paper).

RESULTS AND DISCUSSION

Morphology and Crystal Characterization

After device fabrication, we conducted both SEM and AFM imaging to observe the geometry and morphology of the suspended β-Ga_2O_3 nanodi

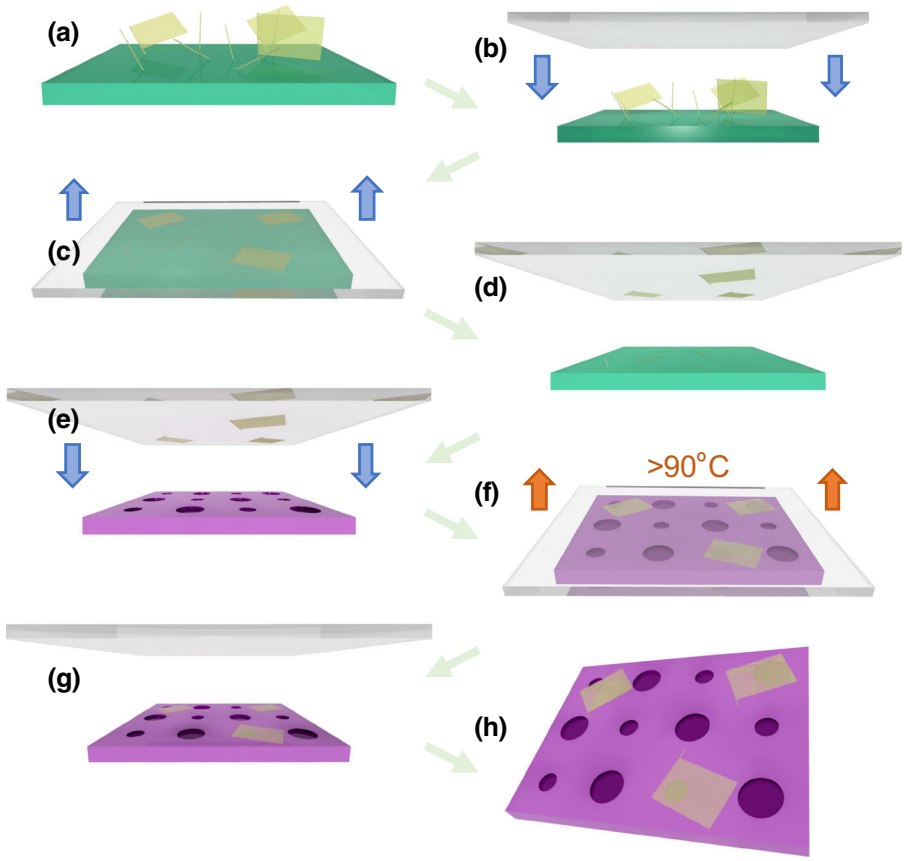

Fig. 1. All-dry transfer process for fabrication of free-standing β-Ga_2O_3 nanodiaphragms: (a) synthesized β-Ga_2O_3 nanorods and nanoflakes on 3C-SiC epilayer, (b) application of thermal release tape, (c) picking up β-Ga_2O_3 nanoflakes by thermal release tape, (d) picked-up β-Ga_2O_3 nanoflakes and nanorods, (e) applying tape with β-Ga_2O_3 nanoflakes to desired substrate with predefined circular microtrenches, (f) releasing nanoflakes at temperature $>$ 90°C, (g) released β-Ga_2O_3 nanoflakes on substrate, and (h) fabricated free-standing β-Ga_2O_3 nanodiaphragms.

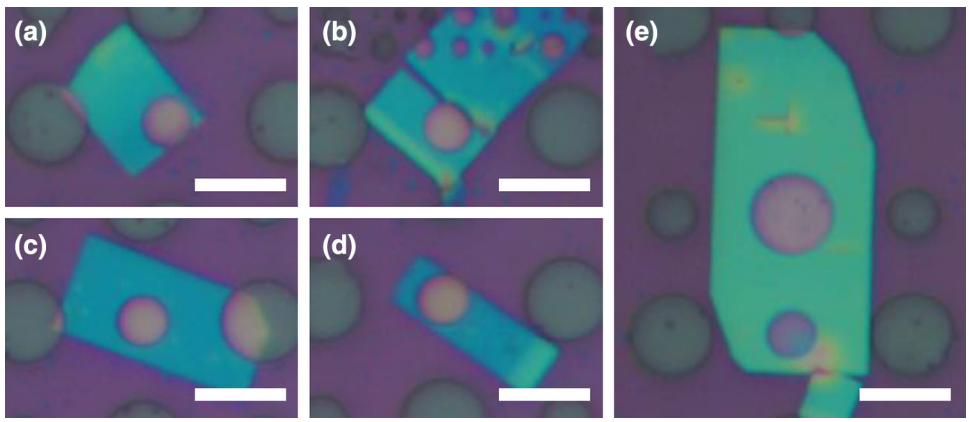

Fig. 2. Optical microscopy images of suspended β-Ga_2O_3 nanodiaphragms: (a) device #1, (b) device #4, (c) device #5, (d) device #6, and (e) device #8. Scale bars: 5 μm.

aphragm structures. Figure 3 presents an SEM image of typical suspended β-Ga_2O_3 nanodiaphragms. Two β-Ga_2O_3 nanoflakes are shown in the image. The small spherical features on and beside the bottom-left flake should be thermal release tape residues. Figure 4 shows an example of the measured AFM morphology, imaged using an Agilent 5500 in tapping mode. The AFM morphology maps also show tape residue features similar to those seen in the SEM image. Based on AFM traces, we extracted the thicknesses of the β-Ga_2O_3 nanodiaphragms as $\sim$20 nm to $\sim$ 80 nm.

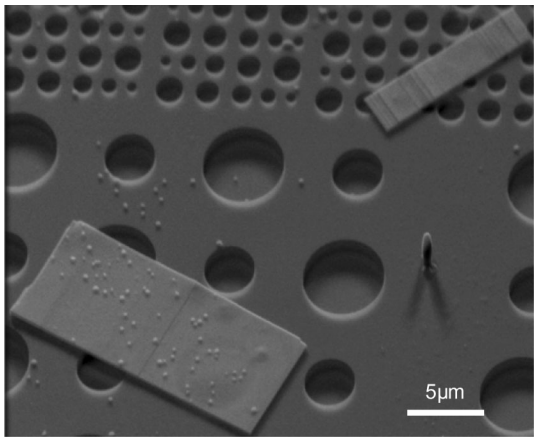

Fig. 3. SEM image of typical suspended β-Ga_2O_3 nanodiaphragms (including device #8, the bottom-left diaphragm in the image).

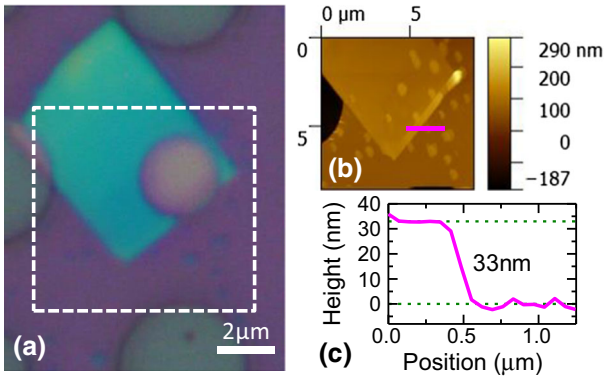

Fig. 4. AFM measurement of device #1. (a) Optical image with white-dashed line box indicating area scanned by AFM. (b) AFM image of indicated area. (c) AFM trace corresponding to magenta line in (b), indicating diaphragm thickness of 33 nm.

We also performed Raman spectroscopy to characterize the crystalline properties of the β-Ga_2O_3 nanoflakes after transfer. A 532-nm laser was focused onto a transferred β-Ga_2O_3 flake using a 50× microscope objective. The typical laser spot diameter was ~ 1 μm. Raman scattered light from the sample was collected in backscattering geometry then guided to a spectrometer (Horiba iHR550) with a 2400 g mm^{-1} grating and 2 min integration time. The Raman signal was recorded using a liquid-nitrogen-cooled charge-coupled device (CCD). The spectral resolution of our system is ~ 1 cm^{-1}. We measured Raman signals from four different locations on the β-Ga_2O_3 nanoflake. We observed Raman modes at 143 cm^{-1}, 168 cm^{-1}, 199 cm^{-1}, 346 cm^{-1}, 416 cm^{-1}, 476 cm^{-1}, and 653 cm^{-1} (Fig. 5) from our device, in very good agreement with the Raman modes of bulk single-crystal β-Ga_2O_3,[33] confirming the high crystal quality of the β-Ga_2O_3 nanoflakes after the transfer

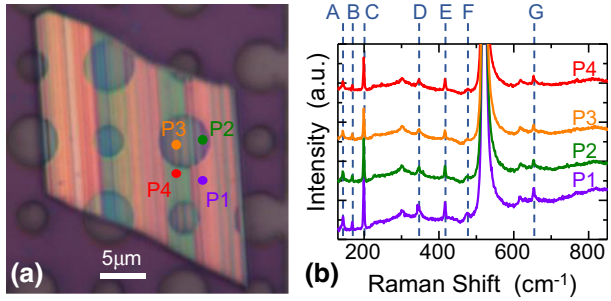

Fig. 5. Typical Raman spectra measured from suspended β-Ga_2O_3 nanodiaphragm after dry transfer. (a) Optical image of diaphragm, with color spots indicating Raman measurement points. (b) Raman spectra from four measured spots of β-Ga_2O_3 crystal, with β-Ga_2O_3 peaks at positions 143 cm^{-1} (A), 168 cm^{-1} (B), 199 cm^{-1} (C), 346 cm^{-1} (D), 416 cm^{-1} (E), 476 cm^{-1} (F), and 653 cm^{-1} (G).

process. In addition, the signals measured from four different locations on the same diaphragm are almost identical to each other, indicating very uniform crystal quality over the β-Ga_2O_3 nanoflake.

Resonances of Vibrating Diaphragms

We measured the characteristics of the fabricated free-standing β-Ga_2O_3 nanodiaphragms by exploiting the nanomechanical resonances of suspended vibrating diaphragms. We employed a custom-built, specially engineered ultrasensitive laser interferometry and photodetection system (Fig. 6) to optoelectronically transduce the minuscule motion of the free-standing β-Ga_2O_3 nanodiaphragms. A 633-nm He–Ne laser was focused onto the suspended β-Ga_2O_3 flake to detect the motion-modulated interference between multiple light reflections from the vacuum–diaphragm, diaphragm–cavity, and cavity–Si interfaces, which was read out using a low-noise photodetector. The depth of the cavity, which is approximately equal to the depth of the microtrench, is around 290 nm. A spectrum analyzer was used to record the signal from the photodetector. We applied incident laser power of ~ 2.8 mW to the devices kept in moderate-vacuum condition (~ 20 mTorr) to ensure good signal-to-noise ratio while avoiding the devices becoming overheated by the laser. Without external driving, the resonators vibrated at their resonances due to undriven thermomechanical motion. The displacement of the thermomechanical motion is on fm/$Hz^{-1/2}$ to pm/$Hz^{-1/2}$ scale. Thanks to its excellent displacement sensitivity, our customized optical interferometry system could discern such small displacements. Figure 7a shows measured multimode resonances of a suspended β-Ga_2O_3 diaphragm (device #7) with thickness of 23 nm and diameter of 5.7 μm. We observed a total of six resonance peaks in the frequency range from ~ 9 MHz to 36 MHz with Q factor of ~ 220 to 280.

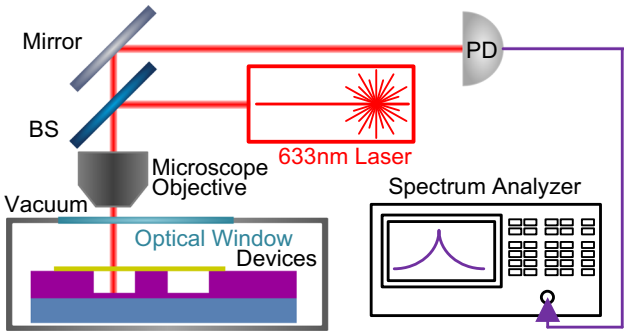

Fig. 6. Optical interferometry measurement apparatus for detection of undriven thermomechanical motion of free-standing β-Ga_2O_3 diaphragm.

After resonance measurements, we performed a thermal annealing process on the suspended β-Ga_2O_3 nanodiaphragms to remove residues and adsorbates on the device surface. During annealing, the devices were placed in a 1-inch quartz-tube furnace with N_2 gas environment at pressure level of $\sim$ 500 mTorr. The temperature was elevated to 250°C and maintained for 1.5 h. Note that this annealing temperature is still much lower than the melting temperature of β-Ga_2O_3 (1820°C),[17] so such thermal annealing should not affect or modify the crystal quality or elastic properties of the β-Ga_2O_3 nanodiaphragms. After annealing, we quickly transferred the device into the vacuum chamber of the optical interferometry system and promptly measured the multimode thermomechanical motion again. We found resonance frequencies ranging from $\sim$ 18 MHz to 53 MHz, exhibiting large upshifts of the resonance frequencies. These effects of annealing on the resonance characteristics can be attributed to elimination of added mass and surface loss pathways arising from thermal release tape residues and gas adsorbates (e.g., O_2 gas molecules) on the device surface. To discern effects due to these two possible effects (i.e., residues and gas adsorbates), we kept the device for over 1 month in moderate vacuum ($\sim$ 70 Torr) at room temperature. This process only adds gas adsorbates onto the device while the amount of fabrication residues remaining after the first annealing remains invariant. After 1 month of exposure to moderate vacuum, the multimode resonances were measured again, showing considerable frequency downshifts from $\sim$ 3% to 15%. This observation indicates that β-Ga_2O_3 can adsorb gas molecules efficiently even in moderate vacuum and that the NEMS device platform is sensitive enough to detect the added adsorbates. We further conducted a second annealing process under the same condition (T = 250°C and N_2 gas under $p \approx$ 500 mTorr) and measured the resonance characteristics again. We found that the resonance frequencies were then slightly higher than those after the first annealing processing, indicating refreshing of the device from surface adsorbates and further removal of remaining tape residues after the first annealing process.

Displacement Sensitivity

Since the gas adsorbates and possible tape residues were largely removed through the thermal annealing processes, we modeled the dynamic motion of the β-Ga_2O_3 nanodiaphragms using the material properties of β-Ga_2O_3 and the environmental temperature. Such analysis can be used to calibrate the responsivity and sensitivity of the interferometry system from mechanical displacement to electrical signal. We calculated the thermomechanical noise in the displacement domain using[34]

$$S_{x,\mathrm{th}}^{1/2}(\omega) = \left(\frac{4k_\mathrm{B}T\omega_m}{M_{m,\mathrm{eff}} \cdot Q_m} \cdot \frac{1}{(\omega^2 - \omega_m^2)^2 + (\omega\omega_m/Q_m)^2} \right)^{1/2}. \tag{1}$$

When the device is on resonance ($\omega = \omega_m$), this expression simplifies to

$$S_{x,\mathrm{th}}^{1/2}(\omega_m) = \left(\frac{4k_\mathrm{B}TQ_m}{\omega_m^3 M_{m,\mathrm{eff}}} \right)^{1/2}, \tag{2}$$

where ω_m, k_B, T, Q_m, and $M_{m,\mathrm{eff}}$ are the angular resonance frequency, Boltzmann constant, temperature, quality factor, and effective mass, respectively, and m denotes the mth resonance mode of the suspended diaphragm.

To derive the effective mass of the suspended diaphragm, we started by calculating the kinetic energy of the system as

$$E = \iint_m \frac{1}{2} u_m^2 \mathrm{d}m, \tag{3}$$

where u_m is the velocity distribution of the mth resonance mode of the diaphragm, given by

$$u_m(x,y) = \frac{z_m(x,y)}{z_{m,\max}} \dot{z}, \tag{4}$$

where $z_m(x,y)$ is the mode shape of the mth mode, $z_{m,\max}$ is the maximum displacement of the mth mode, and $\dot{z}$ is the lumped velocity. Substituting Eq. 4 into Eq. 3 yields

$$E = \frac{1}{2} M \cdot \frac{\int_S z_m^2(x,y)\mathrm{d}S}{\pi a^2 \cdot z_{m,\max}^2} \cdot \dot{z}^2 = \frac{1}{2} M_{m,\mathrm{eff}} \dot{z}^2, \tag{5}$$

where M is the device mass, a is the radius, and $M_{m,\mathrm{eff}}$ is the effective mass of the mth mode. From Eq. 5, the effective mass can be calculated as

$$M_{m,\mathrm{eff}} = \frac{\int_S z_m^2(x,y)\mathrm{d}S}{\pi a^2 \cdot z_{m,\max}^2} M. \tag{6}$$

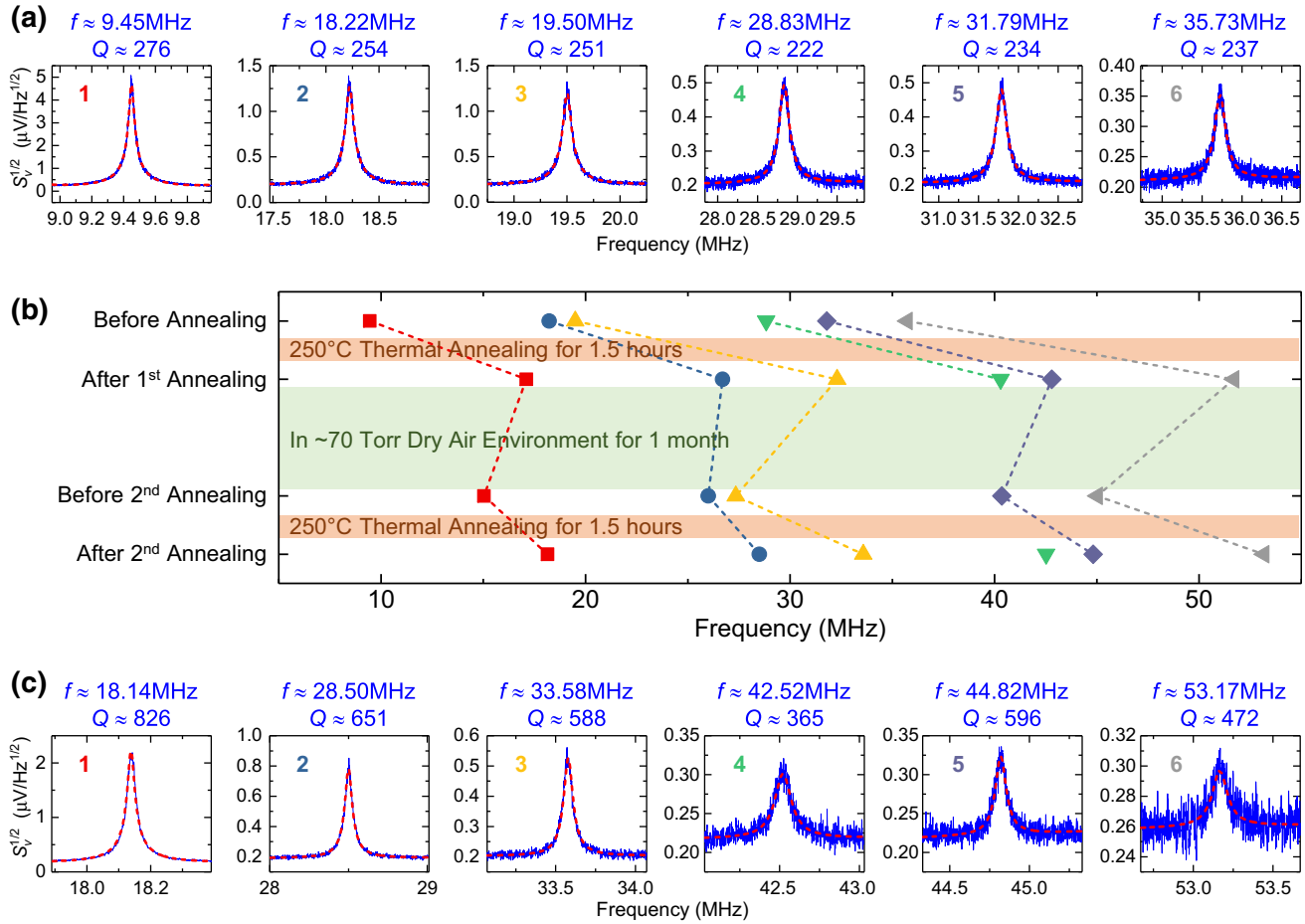

Fig. 7. Effects of annealing on β-Ga_2O_3 nanodiaphragm (device #7). (a) Undriven thermomechanical mode resonance spectra of first six modes before all annealing with corresponding frequencies and Q factors. (b) Resonance frequencies of device #7 before annealing, after first annealing, after $\sim$ 1 month kept in $\sim$ 70 Torr desiccator environment, and after second thermal annealing. (c) Undriven thermomechanical modes resonance spectra of first six modes immediately after second annealing, with corresponding resonance frequencies and Q factors.

For thick enough devices (in "disk" regime), the deflection for the fundamental mode as a function of radial position r ($0 \le r \le a$) is given as[35]

$$z_0(r) = J_0(k_0 r) - \frac{J_0(k_0 a)}{I_0(k_0 a)} \cdot I_0(k_0 r), \qquad (7)$$

where J_0 is the zeroth-order Bessel function J, I_0 is the zeroth-order extended Bessel function I, and $(k_m a)^2$ is the eigenvalue, e.g., $(k_0 a)^2 = 10.215$ for the fundamental mode of the disk resonator. According to Eq. 6, the fundamental mode effective mass of a "disk" regime diaphragm is $M_{0,\mathrm{eff}} = 0.1828M$. The effective masses of thinner devices (devices #7 and #10) can be calculated by incorporating finite element method (FEM)-simulated mode shapes into Eq. 6.

We assumed that the laser heating was minimal, as the photon energy of the 633-nm laser (1.96 eV) is much lower than the bandgap of β-Ga_2O_3 (4.5 eV to 4.9 eV) and the device temperature remained at room temperature ($T \approx 300$ K, minimal laser heating). Using the aforementioned analysis from Eqs. 1 to 7, the displacement-domain thermomechanical noise $S_{x,\mathrm{th}}^{1/2}$ of the resonator can be calculated. Furthermore, we determined the responsivity $\Re \equiv S_{v,\mathrm{th}}^{1/2} / S_{x,\mathrm{th}}^{1/2}$ and displacement sensitivity of the optical interferometry system $S_{x,\mathrm{sys}}^{1/2} \equiv S_{v,\mathrm{sys}}^{1/2} / \Re$ for each device. Here, $S_{v,\mathrm{th}}^{1/2}$ and $S_{v,\mathrm{sys}}^{1/2}$ are the voltage-domain thermomechanical noise and the noise level of the measurement system, respectively. For all devices in this work, the responsivities and sensitivities of the interferometry system ranged from 12 μV/pm to 60 μV/pm and from 4 fm/Hz$^{1/2}$ to 19 fm/Hz$^{1/2}$, respectively. Table I summarizes the responsivity and sensitivity of different devices when using the optical interferometry measurement system. Plotting the relations between the responsivity and sensitivity versus the diaphragm diameter and thickness (Fig. 8) reveals that larger and thicker diaphragms tend to show better responsivity and sensitivity. This can be attributed to the greater

Table I. Optical interferometry responsivity and sensitivity

Device no.	Thickness (nm)	Diameter (μm)	Effective mass coeff.	Displacement spectral density (fm/Hz$^{1/2}$)	Voltage-Domain spectral density (μV/Hz$^{1/2}$)	Responsivity (μV/pm)	Sensitivity (fm/Hz$^{1/2}$)
1	33	3.20	0.183	25.18	0.302	12.01	19.14
2	60	3.20	0.183	13.10	0.279	21.33	15.94
3	45	3.32	0.183	26.97	0.574	21.28	12.22
4	47	3.11	0.183	12.52	0.257	20.52	13.65
5	39	3.20	0.183	30.87	0.556	18.02	13.87
6	34	3.65	0.183	25.00	0.427	17.06	12.89
7	23	5.70	0.208	113.27	2.171	19.17	10.44
8	73	5.18	0.183	16.47	0.671	40.74	4.91
9	61	5.24	0.183	21.70	1.312	60.45	3.64
10	42	5.36	0.192	43.37	1.363	31.41	7.00

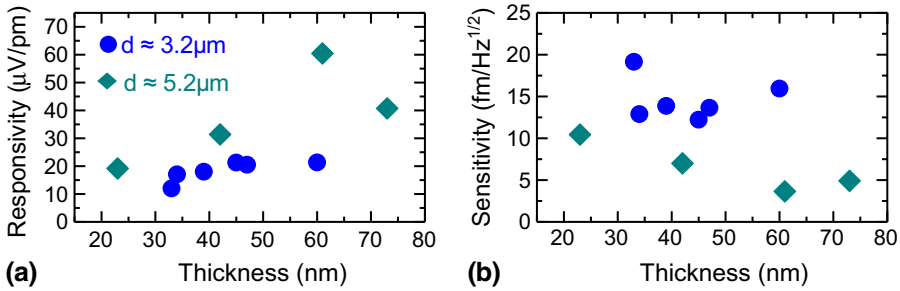

Fig. 8. (a) Responsivities and (b) sensitivities of laser optical interferometry measurement system for suspended β-Ga_2O_3 diaphragms.

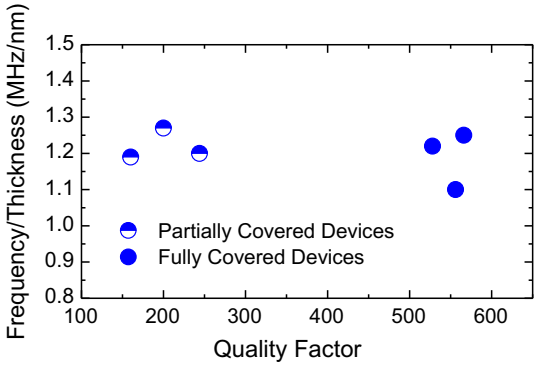

Fig. 9. Device-thickness-normalized fundamental mode resonance frequency versus fundamental mode quality factor for devices #1 to #6. Half-covered symbols represent devices with geometry nonideality, i.e., partially covered diaphragms or diaphragms with thickness step. Filled symbols represent devices fully clamped on circular trenches.

displacement of larger devices and greater light reflectance from thicker diaphragms.

EFFECTS OF STRUCTURAL NONIDEALITIES ON RESONANCES

The resonance characteristics of the β-Ga_2O_3 nanodiaphragms may be affected by structural nonidealities of the devices. Figure 9 shows the effects of structural nonidealities (i.e., partially covered diaphragms or diaphragms with thickness steps in the suspended area, as seen in Fig. 2a or b, respectively) on the resonance frequencies and Q factors for devices #1 to #6. All such nonideal features occupy only a tiny portion of the suspended area. In other words, the nonidealities are rather small compared with the device sizes. Given the size and thickness of these devices (lying in the "disk" regime),[36,37] the resonance frequencies of these devices are governed by the equation[36,37]

$$\omega_m = \frac{t \cdot (k_m a)^2}{a^2} \sqrt{\frac{E_Y}{12\rho(1-\nu^2)}}, \tag{8}$$

where t is the thickness of the nanodiaphragm, a is the radius of the suspended circular area, E_Y is the Young's modulus, ρ is the volume mass density, and ν is the Poisson's ratio of β-Ga_2O_3. This equation indicates that, for devices of given diameter, the resonance frequency is linearly related to the thickness of the diaphragm. Thus, when studying devices with different thicknesses but similar diameters (devices #1 to #6), one can normalize the resonance frequencies of the devices using their thicknesses. The results (Fig. 8) show highly deteriorated Q factors due to minor structural nonidealities but with no clear effect on the resonance frequencies.

Table II. List of devices and their measured parameters

Device #	Diameter, d (μm)	Thickness, t (nm)	Mode #, m	Before annealing		After second annealing	
				Resonance frequency, f_m (MHz)	Quality factor, Q	Resonance frequency, f_m (MHz)	Quality factor, Q
1	3.20	33	1	36.8	170	41.8	200
2	3.20	60	1	65.5	420	74.9	566
3	3.32	45	1	41.7	310	49.4	556
4	3.11	47	1	49.1	107	56.0	160
5	3.20	39	1	37.7	200	47.7	528
6	3.65	34	1	30.8	161	40.7	244
7	5.70	23	1	9.5	276	18.1	826
			2	18.2	254	28.5	651
			3	19.5	251	33.6	588
			4	28.8	222	42.5	365
			5	31.8	234	44.8	596
			6	35.7	237	53.1	472
8	5.18	73	1	27.0	163	33.0	244
			2	55.5	237	–	–
9	5.24	61	1	21.2	354	39.6	626
			2	43.5	371	–	–
			3	45.4	295	–	–
10	5.36	42	1	15.9	162	23.5	395
			2	33.3	263	41.7	268
			3	–	–	45.7	505

Since Q^{-1} represents the dissipation rate of a mechanical resonator, the lower the Q factor of a mechanical resonator, the lossier it is. These results therefore indicate that minor structural imperfections act as a major dissipation pathway for this kind of nanomechanical device.

CONCLUSIONS

We present the first free-standing, very thin β-Ga_2O_3 diaphragms obtained from single-crystal β-Ga_2O_3 nanoflakes grown on 3C-SiC via LPCVD. The suspended β-Ga_2O_3 diaphragms naturally make circular drumheads with thicknesses of 23 nm to 73 nm and diameters of ~ 3.2 μm and ~ 5.2 μm. The multimode resonance characteristics of these circular diaphragms were investigated using an ultrasensitive optical interferometry system, yielding multimode resonances in the range from ~ 10 MHz to 75 MHz. The effects of thermal annealing on the resonance characteristics were measured, revealing that β-Ga_2O_3 can adsorb gas molecules from air efficiently and that the free-standing β-Ga_2O_3 nanostructure platform may help resolve and quantify such adsorbates based on resonance frequency shifts stemming from mass-loading effects, with the potential for restoration and refreshing of the surface by heating. Table II summarizes the resonant characteristics of all the devices before annealing and after the second annealing. Not only have free-standing β-Ga_2O_3 diaphragms been realized, but this work also shows that these β-Ga_2O_3 nanomechanical structures may enable future devices with potential use in gas sensing applications.

ACKNOWLEDGEMENTS

We thank the US Department of Energy (DOE, EERE Grant DE-EE0006719), the National Science Foundation (SNM Award, Grant CMMI-1246715), and the Great Lakes Energy Institute (GLEI, ThinkEnergy Fellowship, X.Q. Zheng) for financial support. S. Rafique, L. Han and H. Zhao thank the National Science Foundation (DMR Grant, DMR-1755479) for financial support. L. Han and H. Zhao thank the National Science Foundation (CNS Grant, CNS-1664368) for financial support. Part of the device fabrication was performed at the Cornell NanoScale Science and Technology Facility (CNF), a member of the National Nanotechnology Infrastructure Network (NNIN), supported by the National Science Foundation (Grant ECCS-0335765).

REFERENCES

1. K. Shenai, M. Dudley, and R.F. Davis, *ECS J. Solid State Sci. Technol.* 2, N3055 (2013).
2. V. Cimalla, J. Pezoldt, and O. Ambacher, *J. Phys. D Appl. Phys.* 40, 6386 (2007).
3. A.J. Green, K.D. Chabak, E.R. Heller, R.C. Fitch, M. Baldini, A. Fiedler, K. Irmscher, G. Wagner, Z. Galazka, S.E. Tetlak, A. Crespo, K. Leedy, and G.H. Jessen, *IEEE Electron Device Lett.* 37, 902 (2016).
4. M. Higashiwaki, K. Sasaki, H. Murakami, Y. Kumagai, A. Koukitu, A. Kuramata, T. Masui, and S. Yamakoshi, *Semicond. Sci. Technol.* 31, 034001 (2016).
5. H. Zhou, M. Si, S. Alghamdi, G. Qiu, L. Yang, and P.D. Ye, *IEEE Electron Device Lett.* 38, 103 (2017).
6. R. Zou, Z. Zhang, Q. Liu, J. Hu, L. Sang, M. Liao, and W. Zhang, *Small* 10, 1848 (2014).

7. W.-Y. Kong, G.-A. Wu, K.-Y. Wang, T.-F. Zhang, Y.-F. Zou, D.-D. Wang, and L.-B. Luo, *Adv. Mater.* 28, 10725 (2016).
8. M.R. Lorenz, J.F. Woods, and R.J. Gambino, *J. Phys. Chem. Solids* 28, 403 (1967).
9. N. Ueda, H. Hosono, R. Waseda, and H. Kawazoe, *Appl. Phys. Lett.* 71, 933 (1997).
10. T. Kimoto and J.A. Cooper, *Fundamentals of Silicon Carbide Technology: Growth, Characterization, Devices, and Applications* (Singapore: Wiley, 2014).
11. J.L. Hudgins, G.S. Simin, E. Santi, and M. Asif Khan, *IEEE Trans. Power Electron.* 18, 907 (2003).
12. T. Oishi, Y. Koga, K. Harada, and M. Kasu, *Appl. Phys. Express* 8, 031101 (2015).
13. M. Higashiwaki, K. Sasaki, A. Kuramata, T. Masui, and S. Ymakoshi, *Appl. Phys. Lett.* 100, 013504 (2012).
14. K.D. Chabak, N. Moser, A.J. Green, D.E. Walker Jr, S.E. Tetlak, E. Heller, A. Crespo, R. Fitch, J.P. McCandless, K. Leedy, M. Baldini, G. Wagner, Z. Galazka, X. Li, and G. Jessen, *Appl. Phys. Lett.* 109, 213501 (2016).
15. M.-F. Yu, M.Z. Atashbar, and X. Chen, *IEEE Sens. J* 5, 20 (2005).
16. V.I. Nikolaev, V. Maslov, S.I. Stepanov, A.I. Pechnikov, V. Krymov, I.P. Nikitina, L.I. Guzilova, V.E. Bougrov, and A.E. Romanov, *J. Cryst. Growth* 457, 132 (2017).
17. Z. Galazka, R. Uecker, K. Irmscher, M. Albrecht, D. Klimm, M. Pietsch, M. Brützam, R. Bertram, S. Ganschow, and R. Fornari, *Cryst. Res. Technol.* 45, 1229 (2010).
18. R. Jangir, S. Porwal, P. Tiwari, P. Mondal, S.K. Rai, T. Ganguli, S.M. Oak, and S.K. Deb, *J. Appl. Phys.* 112, 034307 (2012).
19. Y. Tomm, P. Reiche, D. Klimm, and T. Fukuda, *J. Cryst. Growth* 220, 510 (2000).
20. N. Ueda, H. Hosono, R. Waseda, and H. Kawazoe, *Appl. Phys. Lett.* 70, 3561 (1997).
21. Y. Tomm, J.M. Ko, A. Yoshikawa, and T. Fukuda, *Sol. Energy Mater. Sol. Cells* 66, 369 (2001).
22. E.G. Villora, K. Shimamura, Y. Yoshikawa, K. Aoki, and N. Ichinose, *J. Cryst. Growth* 270, 420 (2004).
23. S. Rafique, L. Han, M.J. Tadjer, J.A. Freitas Jr, N.A. Mahadik, and H. Zhao, *Appl. Phys. Lett.* 108, 182105 (2016).
24. S. Rafique, L. Han, A.T. Neal, S. Mou, M.J. Tadjer, R.H. French, and H. Zhao, *Appl. Phys. Lett.* 109, 132103 (2016).
25. S. Kumar, G. Sarau, C. Tessarek, M.Y. Bashouti, A. Hähnel, S. Christiansen, and R. Singh, *J. Phys. D Appl. Phys.* 47, 435101 (2014).
26. J. Zhang, F. Jiang, Y. Yang, and J. Li, *J. Phys. Chem. B* 109, 13143 (2005).
27. S. Rafique, L. Han, C.A. Zorman, and H. Zhao, *Cryst. Growth Des.* 16, 511 (2016).
28. S. Ohira, T. Sugawara, K. Nakajima, and T. Shishido, *J. Alloys Compd.* 402, 204 (2005).
29. S. Rafique, L. Han, J. Lee, X.-Q. Zheng, C.A. Zorman, P.X.-L. Feng, and H. Zhao, *J. Vac. Sci. Technol. B* 35, 011208 (2017).
30. R. Mitdank, S. Dusari, C. Bülow, M. Albrecht, Z. Galazka, and S.F. Fischer, *Phys. Status Solidi A* 211, 543 (2014).
31. J. Kim, S. Oh, M.A. Mastro, and J. Kim, *Phys. Chem. Chem. Phys.* 18, 15760 (2016).
32. Y. Kwon, G. Lee, S. Oh, J. Kim, S.J. Pearton, and F. Ren, *Appl. Phys. Lett.* 110, 131901 (2017).
33. C. Kranert, C. Sturm, R. Schmidt-Grund, and M. Grundmann, *Sci. Rep.* 6, 35964 (2016).
34. Z. Wang, J. Lee, and P.X.-L. Feng, *Nat. Commun.* 5, 5158 (2014).
35. K.F. Graff, *Wave Motion in Elastic Solids* (New York: Dover, 1991).
36. H. Suzuki, N. Yamaguchi, and H. Izumi, *Acoust. Sci. Technol.* 30, 348 (2009).
37. J. Lee, Z. Wang, K. He, J. Shan, and P.X.-L. Feng, *ACS Nano* 7, 6086 (2013).